Encapsulin nanocontainers as versatile scaffolds for the development of artificial metabolons

Matthew C. Jenkins[§], Stefan Lutz^{¶*}

Department of Chemistry, Emory University, Atlanta, Georgia, 30084, United States.

[§] School of Chemistry and Biochemistry, Georgia Institute of Technology, Atlanta, Georgia 30306, United States.

[¶] Codexis Inc., 200 Penobscot Drive, Redwood City, California 94063, United States.

ABSTRACT

The construction of non-native biosynthetic pathways represents a powerful, modular strategy for the production of valuable synthons and fine chemicals. Accordingly, artificially affixing enzymes that catalyze sequential reactions onto DNAs, proteins, or synthetic scaffolds has proven to be an effective route for generating de novo metabolons with novel functionalities and superior efficiency. In recent years, nanoscale microbial compartments known as encapsulins have emerged as a class of robust and highly engineerable proteinaceous containers with myriad applications in biotechnology and synthetic biology. Herein we report the concurrent surface functionalization and internal packaging of encapsulins from Thermotoga maritima to generate a catalytically competent two-enzyme metabolon. Encapsulins were engineered to covalently sequester up to 60 copies of a dihydrofolate reductase (DHFR) enzyme variant on their exterior surfaces using the SpyCatcher bioconjugation system while their lumens were packaged with a tetrahydrofolate-dependent demethylase enzyme using short peptide affinity tags abstracted from the encapsulin's native protein cargo. Successful cross-talk between the two co-localized enzymes was confirmed as tetrahydrofolate produced by externally tethered DHFR was capable of driving the demethylation of a lignin-derived aryl substrate by packaged demethylases, albeit slowly. The subsequent introduction of a previously reported pore-enlarging deletion in the encapsulin shell was shown to enhance metabolite exchange such that the encapsulin-based metabolon functioned at speeds equivalent to those of the two enzymes freely dispersed in solution. Our work thus further emphasizes the engineerability of encapsulins and their potential use as flexile scaffolds for biocatalytic applications.

KEYWORDS

Encapsulin, nanoreactor, bioconjugation, biocatalysis, SpyCatcher, synthetic biology

INTRODUCTION

Protein-based micro- and nanoscale containers are specialized three-dimensional architectures found throughout nature that are inherently designed to perform a variety of biologically essential tasks, including the packaging, protection, and transportation of genetic material, the generation of chemically distinct microenvironments, the co-localization of functionally-related cellular machinery, and the dynamic regulation of specific metabolites according to cellular needs. ¹⁻⁶ Structural characterizations of proteinaceous containers originating from all kingdoms of life have revealed highly uniform macromolecular assemblies adopting a range of sizes and morphologies, the most common of which include spherical containers displaying polyhedral symmetries and rod-like containers forming extended tubular filaments. ⁷⁻⁹ Assembled containers are typically generated from the polymerization of one or more protomeric subunits, and, in accordance with their diverse native functions, generally display unique biophysical properties. As a result of their natural polyvalency, monodispersity, structural plasticity, and biocompatibility, protein containers have attracted increasing attention over the last half century as functionalizable nanoscale vehicles for applications in medicine, industrial catalytic processes, and the development of next-generation biomaterials. ⁹⁻¹¹

In nature, both eukaryotic and prokaryotic organisms rely on multistep enzymatic cascade reactions to rapidly facilitate the numerous cellular processes necessary to sustain life and growth. ¹² Enzymatic cascades are inherently beneficial as they allow organisms to maintain lower net concentrations of metabolic intermediates, thus preventing the formation of futile byproducts or the release of toxic species into the larger cellular environment. ^{13, 14} Further, metabolic cascades can often enhance the individual reactivities and selectivities of pathway enzymes through a process known as "substrate channeling" in which normal reaction equilibria are subverted through the direct transfer of intermediates between sequentially acting enzyme catalysts. ^{13, 15} For efficient substrate channeling to occur, however,

functionally related enzymes must typically be co-localized within macromolecular complexes or organelle structures to minimize the spatial distances chemical intermediates must traverse between active sites.¹⁶

Chemists and synthetic biologists alike have devoted intense research efforts towards mimicking the co-localization properties of natural systems using synthetically crafted multienzyme metabolons. Generally, synthetic enzyme complexes have been constructed using a number of related strategies including the generation of non-native fusion proteins^{17, 18}, using protein or DNA-based scaffolds as selective enzyme templates¹⁹⁻²⁴, the immobilization of enzymes onto solid supports²⁵⁻²⁷, or by sequestering enzymes within lipid-bound micelles or proteinaceous cages²⁸⁻³⁵. In recent decades, naturally occurring protein-based cage assemblies, including bacterial microcompartments and virus-like particles derived from various viral species, have been increasingly utilized for the development of artificial metabolons due to their uniform sizes, engineerability and their capacity to serve as both nanoscale containers and as functionalizable templates^{1, 36, 37}. Accordingly, several exciting examples in the last few years have illustrated either the covalent scaffolding of multienzyme systems on nanocontainer surfaces or the encapsulation of multiple enzymes within container luminal spaces, producing nano-scaffolds serving as high sensitivity biosensors^{38, 39}, and as biocatalytic platforms for the production of therapeutic synthons⁴⁰, biofuel precursors^{41, 42}, and commercially relevant fabric dyes⁴³.

Within the last two decades, a new class of protein-based microbial nanocontainers known as encapsulins have emerged. Similar to bacterial microcompartments and viral capsids, encapsulins are polyhedral shells constructed in a homopolymeric fashion from single coat proteins adopting the prototypical fold of the gp5 major capsid protein from the HK97 bacteriophage. ^{44, 45} Atomic resolution structures obtained in recent years for several encapsulins of bacterial and archaeal origin reveal cage assemblies on the order of 20 to 42 nm in external diameter that are constructed from 60, 180 or 240

Currently, encapsulin containers are believed to function as pseudo-organelles participating in the intracellular mitigation of oxidative stressors as they have been found to selectively encapsulate enzyme cargoes including dye-decolorizing peroxidases, ferritin-like iron mineralizing proteins, haemerythrins, and two-domain nitrite reductase-hydroxylamine oxidases.^{6, 44, 50} Cargo encapsulation is predominantly effected *in vivo* via short aliphatic localization peptides presented on one of the cargo protein's termini that bind within defined hydrophobic clefts located on the luminal faces of each encapsulin coat protein. Subsequent metabolite exchange between the encapsulated cargo and the exterior spaces occurs through a series of largely conserved pores localized to the containers' 2-fold, 3-fold, and 5-fold symmetry axes.⁴⁴

In recent years, several studies have shown that encapsulin cargo-loading peptides (Clps) can be used to direct the encapsulation of non-native cargoes, including reporter proteins 51,52 , enzymes 53,54 , and inorganic nanoparticles 55 , within the lumen of assembled nanocontainers. Accordingly, encapsulins have become attractive candidates for the development of tailored, biorthogonal protein scaffolds for varied biotechnology applications. Herein we expand upon these previous works to report the development of a synthetic, nanocontainer-based metabolon using the encapsulin from the hyperthermophilic bacterium *Thermotoga maritima* as a bifunctional scaffold for the co-localization of two metabolically compatible enzyme biocatalysts. *Thermotoga maritima* encapsulins (TmEs) natively assemble from 60 copies of a 30.5 kDa protein monomer, adopting uniform macromolecular cage structures adhering to a T=1 symmetry model with internal and external diameters of approximately 20 and 24 nm, respectively. For our proof-of-principle metabolon, we chose to couple the enzymatic activities of a recently identified aryl-O-demethylase, LigM, from the soil bacterium *Sphingomonas paucimobilis* SYK-6 and the dihydrofolate reductase (DHFR) of *Escherichia coli*. LigM represents one of several functionally similar demethylases that have received increasing attention from industrial chemists over the last decade due to their ability to

catabolize mono- and biaryl substrates generated from the degradation of lignin biomass. ^{56, 57} While other demethylases from the lignin catabolism pathway in *S. paucimobilis* SYK-6 use iron or flavin-dependent oxygenases to conduct aryl demethylation, however, LigM catalyzes the demethylation of the monoaryl substrates vanillate and 3-*O*-methylgallate using tetrahydrofolate (THF) as a methyl-acceptor cofactor. ⁵⁷ For the purposes of our metabolon design, we thus reasoned that we could utilize DHFR to generate THF *in situ* from the precursor cofactor dihydrofolate (DHF) to fuel the demethylase activity of LigM in order to probe our metabolon design. To produce our synthetic metabolon, artificial co-localization of the two biocatalysts was accomplished by first packaging LigM enzymes within the encapsulin lumen *in vivo* using the C-terminal Clp abstracted from TmE's native ferritin-like protein cargo followed by covalently decorating the nanocontainers' exterior surfaces with DHFR enzymes *in vitro* using the SpyCatcher/SpyTag bacterial superglue system. ⁵⁸ We subsequently explored the functional consequences of our scaffold design on the catalytic throughput of our metabolon. Our work further exemplifies the robustness of encapsulins as viable nanoscale platforms for the user-defined co-localization of disparate, yet compatible catalysts.

RESULTS AND DISCUSSION

External decoration of encapsulins via isopeptide bonds

As a first step in the production of a nanocontainer-based metabolon, we sought to decorate the exterior of TmE encapsulins, using the SpyCatcher/SpyTag bacterial superglue system derived from the CnaB2 domain of the *Streptococcus pyogenes* fibronectin binding protein FbaB⁵⁸ as a means of covalently tethering biocatalysts uniformly across the nanocontainer surfaces. External presentation of SpyCatcher domains was accomplished by fusing the SpyCatcher gene sequence onto the C-terminus of the TmE monomer gene to form the TmE-SpyCatcher (TmE-SC) hybrid (**Figure 1A** and **1B**). The TmE C-terminus

was chosen for the SpyCatcher domain fusion as it is solvent-exposed in the assembled nanocontainer structure, and because the C-termini of adjacent monomers are spaced roughly 3 nm apart from one another in a pentagonal arrangement around the nanocontainer's 5-fold vertices, which we reasoned should provide sufficient space for decoration with SpyTag-containing biocatalysts (**Figure S1**). Purified TmE-SC fusion proteins were morphologically assessed via transmission electron microscopy (TEM) and were found to be visually indistinguishable from native TmE nanocontainers (**Figure 1C** and **Figure S2**). This result is consistent with previous reports in which the SpyCatcher domain was not visible on the surfaces of similarly sized P22 VLP nanocontainers due to the combination of its small size (12.4 kDa), the negative staining conditions, and the accelerating voltages used for visual assessment during TEM imaging. ⁵⁹

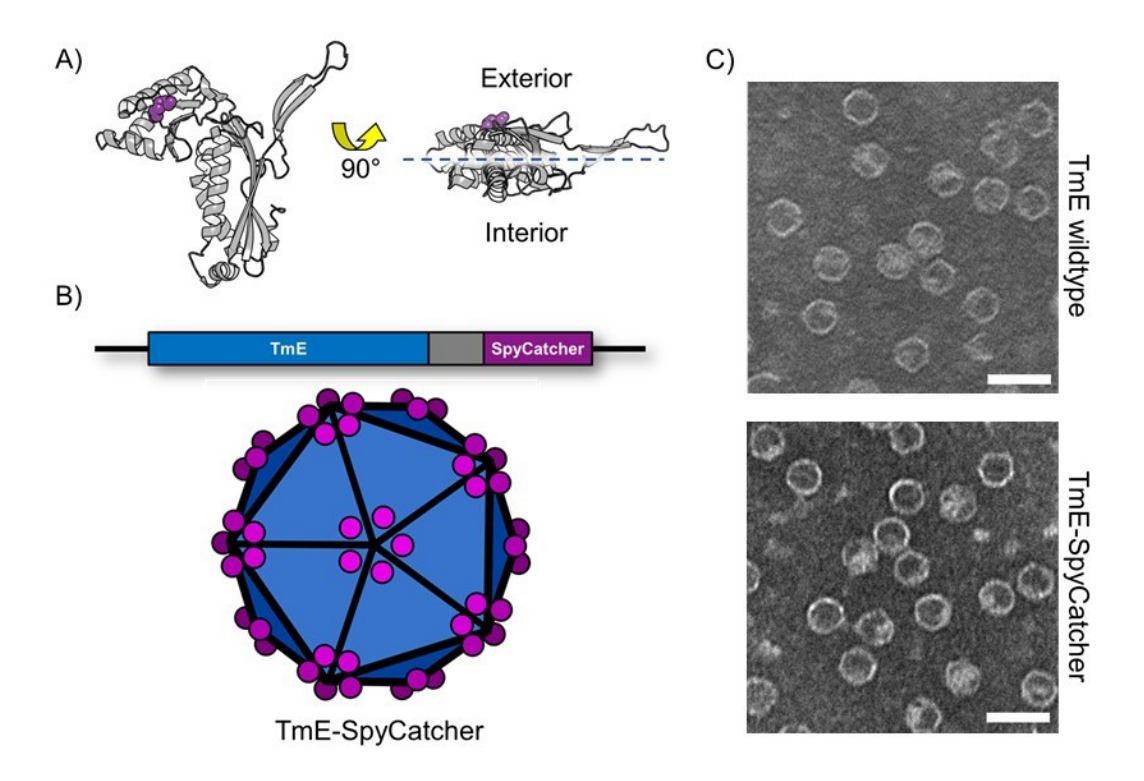


Figure 1. Design of the TmE-SpyCatcher variant nanocontainer. A) Atomic structure of the TmE monomeric subunit with the interior and exterior faces denoted. The monomer's C-terminus (purple spheres) is oriented toward the exterior. B) Cartoon representation of the recombinant TmE-SpyCatcher gene (top) and the corresponding assembled nanocontainer (bottom). The grey box in the gene sequence represents a GSGGGTGGGSGGGTS flexible linker sequence connecting the TmE and SpyCatcher genes. The SpyCatcher domains are represented on the nanocontainer surface as spheres centered around the container's 5-fold symmetry vertices. C) TEM images collected for wildtype (top) and TmE-SpyCatcher (bottom) nanocontainers. Scale bars = 40 nm.

Having shown that TmE-SpyCatcher hybrids retain the ability to self-assemble into nanocontainers, we next sought to probe the functionality of the encapsulin-bound SpyCatcher domains by recombinantly fusing the AHIVMVDAYKPTK sequence of the corresponding SpyTag ligand onto the N-terminus of a superfolder GFP reporter protein (sfGFP-ST). *In vitro* titration of the 44.0 kDa TmE-SC with purified 29.9 kDa sfGFP-ST resulted in the formation of a higher molecular weight bioconjugate product of approximately 74 kDa in SDS-PAGE tests (Figure 2A), indicating that the TmE-tethered SpyCatcher domains retain their native capacity to form isopeptide bonds with available SpyTag fusion proteins. Covalent capture of sfGFP-ST by TmE-SC was further verified via size exclusion chromatography (SEC) in which a 485 nm absorbance signal, corresponding to the absorbance of the sfGFP chromophore⁶⁰, was observed to elute at the same volume as the bioconjugated protein product (Figure 2B). Subsequent TEM images collected from the SEC-purified bioconjugates (denoted TmE-SC:sfGFP-ST to indicate covalent attachment) show that the nanocontainers lose much of the surface clarity previously observed with both the wildtype and TmE-SC containers, indicative of sfGFP-ST surface attachment.

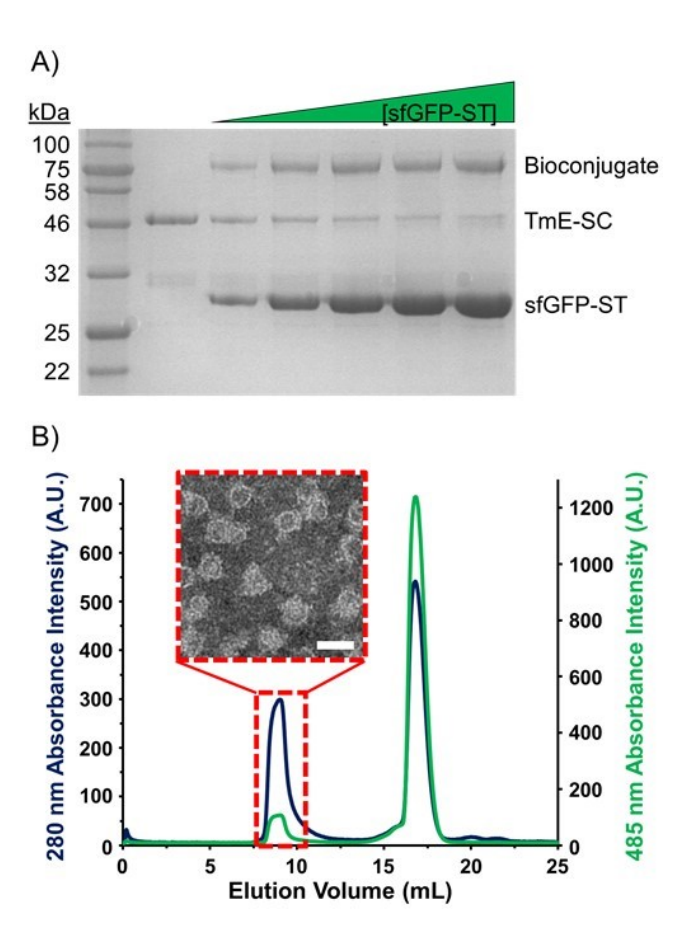


Figure 2. In vitro bioconjugation of TmE-SC and sfGFP-ST. A) Titration of TmE-SC (5 μ M) with increasing concentrations of sfGFP-ST (0 – 10 μ M from left to right in 2 μ M increments) assessed via SDS-PAGE. B) Size-exclusion chromatogram of an *in vitro* mixture of 15 μ M TmE-SC and 20 μ M sfGFP-ST following 1 hour of incubation at 4 °C. The inset TEM image depicts TmE-SC:sfGFP-ST bioconjugate containers isolated from the 8 – 10 mL elution peak. Excess sfGFP-ST elutes later between 16 – 18 mL. TEM scale bar = 40 nm.

Following the successful covalent attachment of sfGFP-ST probes on encapsulin surfaces, the SpyTag sequence was next recombinantly fused onto the N-terminus of *Escherichia coli* dihydrofolate reductase (DHFR-NST) in order to assess the catalytic behavior of nanocontainer-bound enzymes. A subsequent *in vitro* titration of purified TmE-SC with DHFR-NST showed the formation of a similar high molecular weight bioconjugate protein in SDS-PAGE gels as was observed previously during the titration of TmE-SC with sfGFP-ST (**Figure 3A**). To verify that the high molecular weight band indeed arose from the formation of a covalent bond between TmE-SC and DHFR-NST, a mutation was introduced into the SpyTag sequence which has been shown previously to abolish the capacity of the SpyTag to form isopeptide bonds.⁵⁸ Specifically, the SpyTag's sole aspartate residue (D117, SpyCatcher residue

numbering), whose sidechain γ-carbonyl is the target of nucleophilic attack during isopeptide bond formation with the SpyCatcher domain, was converted into an alanine. Repeating the titration experiment with the modified DHFR variant, referred to as DHFR-NST(DA), resulted in a complete lack of bioconjugate formation, confirming that the high molecular weight protein is a product of isopeptide bond formation between the SpyCatcher and SpyTag elements (**Figure 3B**). Likewise, TEM images collected for TmE-SC alone and TmE-SC mixed with DHFR-NST(DA) appear visually identical while images collected for TmE-SC:DHFR-NST bioconjugates show a similar reduction in clarity around the surface of the nanocontainers akin to the TEM images for TmE-SC:sfGFP-ST bioconjugates, though to a seemingly lesser extent (**Figure 3C**).

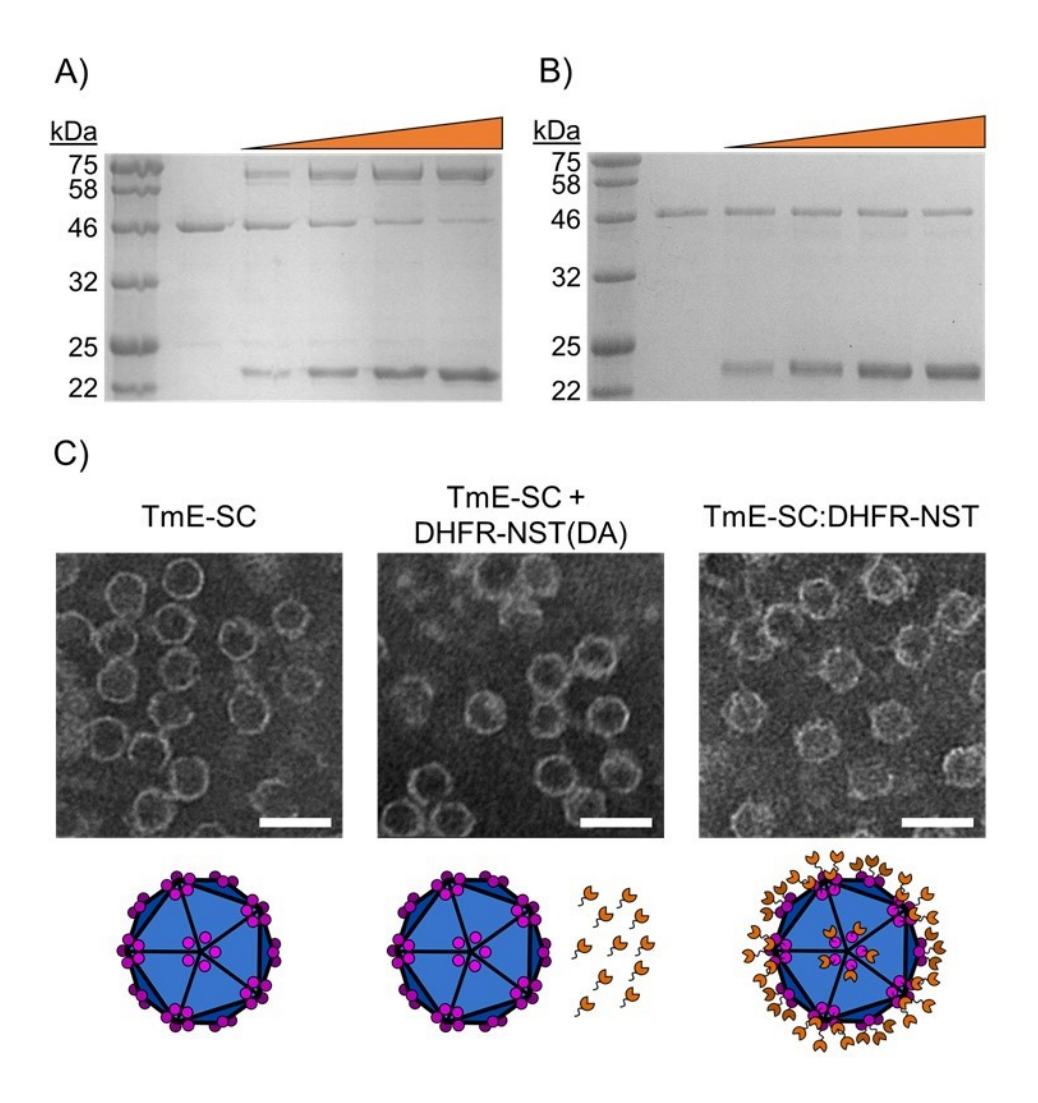


Figure 3. In vitro bioconjugation of TmE-SC with DHFR-NST. Titrations were performed using a fixed concentration of TmE-SC (5 μ M) in the presence of increasing concentrations (0 – 8 μ M from left to right in 2 μ M increments) of either A) DHFR-NST, or B) the same protein containing the DA mutation in the SpyTag to abolish isopeptide bond formation. SDS-PAGE gels were visualized using Coomassie staining. C) TEM images comparing the decorated and non-decorated TmE-SC nanocontainers. Cartoon representations of the contents within each sample are presented below the corresponding TEM images. TEM scale bars = 40 nm.

Michaelis-Menten kinetics of free versus surface-bound DHFR

Initial Michaelis-Menten kinetics monitoring the conversion of dihydrofolate (DHF) to tetrahydrofolate (THF) using DHFR-NST show that the presence of the SpyTag sequence has no appreciable effects on either the enzyme's K_m or k_{cat} values when compared to previous literature reports (**Table 1**). Following this initial assessment, however, we noticed that the enzyme's inherently low Km for DHF (< 1 μ M) necessitated that we conduct our kinetics experiments near the limit of detection

for our spectrophotometric assay. In an attempt to obtain more reliable and reproducible data, we mutated residue 42 of DHFR from the native methionine to a tryptophan (i.e. M42W) as this point mutation has been shown to decrease the enzyme's binding affinity for DHF.62, 64-66 In subsequent kinetic studies, introduction of the M42W mutation into the wildtype DHFR gene lacking the N-terminal SpyTag resulted in a 7-fold increase in the enzyme's K_m to a value of $6.06 \pm 0.67 \mu M$, while introduction of the same mutation into our DHFR(M42W)-SpyTag variant (herein referred to as DHFR*-NST) resulted in an approximately 3-fold increase in K_m to a value of 2.96 \pm 0.33 μM (Figure S3). At this point, we also generated an additional DHFR(M42W) variant with the SpyTag ligand fused onto the enzyme's Cterminus in order to probe whether the orientation of the biocatalyst would influence its catalytic performance upon immobilization onto encapsulin surfaces. This C-terminal variant (DHFR*-CST) was also kinetically characterized, exhibiting a K_m of $6.83 \pm 0.83 \mu M$, a value that is approximately equivalent to the DHFR(M42W) variant without the terminal SpyTag fusion. Interestingly, the k_{cat} values for the DHFR(M42W), DHFR*-NST, and DHFR*-CST variants remained relatively unchanged as compared to the DHFR-NST variant lacking the point mutation (Table 1). Collectively, the unchanged k_{cat} values coupled with the slightly increased K_m values for the M42W variants were sufficient for higher fidelity spectroscopic analyses.

Table 1. Michaelis-Menten kinetics assessments of free and immobilized DHFR variants

	Sample	K _m (μM)	k _{cat} (s ⁻¹)	$k_{cat}/K_m~(\mu M^{-1}s^{-1})$	Fold Change
'	DHFR-NST	0.87 ± 0.04	4.17 ± 0.02	4.79	-
	DHFR-M42W (i.e. DHFR*)	6.06 ± 0.67	4.67 ± 0.14	0.77	↓ 6.2 ^a
N-terminal SpyTag	DHFR*-NST	2.96 ± 0.33	3.98 ± 0.09	1.35	-
	MBP-SC immobilized DHFR*	3.95 ± 0.76	1.77 ± 0.08	0.45	$\downarrow 3.0^b$
	TmE-SC immobilized DHFR*	13.13 ± 1.73	4.49 ± 0.21	0.34	$\downarrow 4.0^b$
	Thrombin-cleaved TmE-SC/DHFR*	4.74 ± 0.65	3.93 ± 0.14	0.83	$\downarrow 1.6^b$
C-terminal SpyTag	DHFR*-CST	6.83 ± 0.83	2.79 ± 0.10	0.41	-
	MBP-SC immobilized DHFR*	6.25 ± 1.18	3.00 ± 0.16	0.48	↑ 1.2°
	TmE-SC immobilized DHFR*	19.74 ± 2.57	2.27 ± 0.12	0.12	$\downarrow 3.4^c$

^aFold change relative to DHFR-NST; ^bFold change relative to DHFR*-NST; ^cFold change relative to DHFR*-CST

We next sought to functionalize TmE-SC nanocontainers with our DHFR*-ST variants and reassess their respective catalytic performances. However, accurately analyzing the kinetic profiles of encapsulins presenting surface-immobilized DHFR* necessitated that the amount of covalently-tethered enzyme in each bioconjugate sample be quantitatively determined. To this end, we found that coexpression of both the TmE-SC and the DHFR*-ST variants in E. coli cells led to the production of nanocontainers with seemingly complete occupancy of the available SpyCatcher domains due to a reproducibly higher in vivo overexpression of the DHFR*-ST variants relative to TmE-SC when the genes for both proteins were induced from T7 promoters (Figure S4). Fully-decorated nanocontainers could subsequently be recovered in high purity from co-expression cultures, permitting the concentration of surface-immobilized DHFR* to be determined spectrophotometrically using the combined theoretical extinction coefficients for the TmE-SC and DHFR*-ST variants as both proteins are present in a 1:1 molar ratio. However, since the spectrophotometric data cannot distinguish between functional and nonfunctional enzymes, we also performed fluorescence-based titrations of our samples using a fluoresceinlabeled derivative of methotrexate (MTX-F), a well-established and potent competitive inhibitor of DHFR.^{67, 68} Specifically, binding of MTX-F within the DHFR active site results in a 3 to 4-fold increase

in fluorescence emission intensity compared to solvent dispersed MTX-F, allowing the population of nanocontainer-bound DHFR enzymes presenting accessible active sites to be abstracted from the titration data. As an example, Figure 4 shows a purified sample of TmE-SC:DHFR*-CST whose concentration was determined to be 4.6 µM from its 280 nm absorbance signal. A portion of this protein sample was diluted to a final concentration of 1.5 μM and was then titrated with MTX-F ranging from 0.2 to 5.0 μM. Segmental regression analysis of the resulting fluorescence titration data yielded an intersection of the two linear trendlines at $1.9 \pm 0.3 \mu M$, which corresponds to a back-calculated concentration of $5.5 \pm 0.9 \mu M$ for the original protein stock. Comparatively, the titration data is in reasonably good agreement with the absorbance data and suggests that all of the encapsulin-bound DHFR* enzymes possess solvent accessible, functional active sites. Additional control reactions confirmed that no detrimental effects on MTX-F binding resulted from either the presence of encapsulin nanocontainers or SpyCatcher domains, or from the formation of isopeptide bonds between DHFR-fused SpyTag peptides and available SpyCatcher domains (Figure S5 and S6). However, given that the spectrophotometric analysis is significantly faster and less error-prone than the MTX-F titration method, we elected to characterize all of the decorated nanocontainers in this manner going forward.

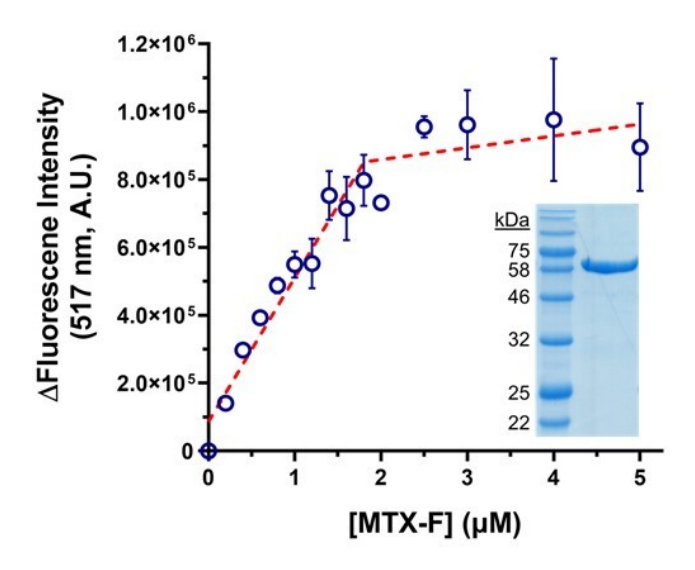


Figure 4. Titration of nanocontainer-bound DHFR* with MTX-F. Purified TmE-SC:DHFR*-CST produced *in vivo* (Coomassie stained SDS-PAGE gel, inset) was diluted to $1.5 \,\mu\text{M}$ and titrated with increasing concentrations of MTX-F ($0-5 \,\mu\text{M}$). The resulting change in fluorescence intensity at 517 nm was used to verify the DHFR* concentration. All data points were collected in triplicate with error bars representing one standard deviation from the mean. Segmental regression fit of data depicted as dashed red lines.

Kinetics data for both DHFR*-ST variants show that immobilization onto TmE surfaces via the SpyCatcher domains has no appreciable effect on the enzymes' k_{cat} values, though 4.4-fold and 2.9-fold increases in K_m for DHF were observed for the DHFR*-NST and DHFR*-CST enzymes, respectively (Table 1). To determine whether these decreases in substrate binding affinity resulted from immobilization of the DHFR* variants onto encapsulins themselves or whether the effect was the result of isopeptide bond formation with another protein in general, the SpyCatcher domain was genetically fused onto the C-terminus of the *E. coli* maltose binding protein (MBP) to generate a MBP-SpyCatcher hybrid (MBP-SC) as a generic covalent binding partner (Figure S7 and S8). Subsequent kinetics tests with purified MBP-SC:DHFR*-ST conjugates showed no significant increase in K_m for either DHFR* variant, indicating that the decrease in DHF binding affinity upon encapsulin-immobilization is a phenomenon that is likely specific to the nanocontainer assemblies. Additionally, the DHFR*-NST variant possesses an encoded thrombin cleavage site interspersed between the SpyTag sequence and the beginning of the DHFR* gene. Encapsulins decorated with DHFR*-NST were kinetically assessed (Table 1) and were then treated with bovine thrombin to liberate the bound DHFR* enzymes (Figure S9). The cleaved

DHFR* enzymes were then isolated via SEC and their kinetic parameters were reassessed for comparison (**Table 1**). The resulting data show that thrombolytic cleavage of DHFR*-NST from the encapsulin surface alleviates the observed decrease in binding affinity for DHF, further indicating that the K_m alterations are specific to encapsulin immobilization. We speculate that the decreased binding affinities possibly arise from steric crowding of the surface-bound DHFR* enzymes, localized environmental perturbations generated in the immediate proximity of the nanocontainers (e.g. solvent viscosity, pH, etc.)⁶⁹⁻⁷¹, or due dynamic interactions between the DHFR* enzymes and the encapsulin surface (resulting from the flexible nature of the linker sequences connecting the TmE and SpyCatcher domains) leading to some percentage of the enzyme population adopting orientations that occlude access to the active site. However, given that the observed K_m increases for DHF are relatively minor, we did not investigate this effect further.

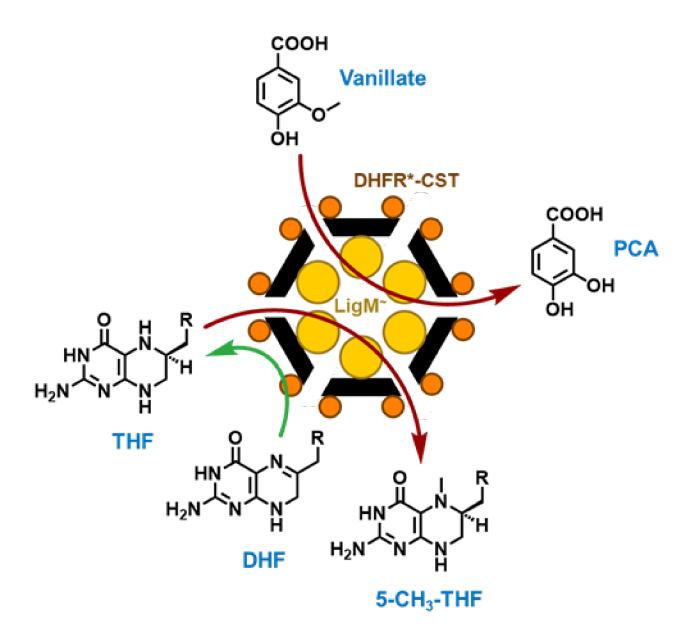


Figure 5. TmE-scaffolded metabolon design. Surface immobilized DHFR* enzymes (represented by orange spheres) are used to generate THF *in situ* from DHF (green reaction arrow) in order to fuel the THF-dependent demethylase activity of encapsulated LigM[~] (yellow spheres) using vanillate as a substrate (dark red reaction arrows). For the folate cofactors above, only the reactive pterin moieties are shown for brevity while the cofactors' *p*-(aminobenzoyl)-L-glutamate moieties are represented as R-groups.

Generation and testing of a synthetic two-enzyme metabolon

Having shown that immobilization of DHFR* variants on encapsulin surfaces is minimally perturbative to the enzymes' respective catalytic functions, we next sought to expand our encapsulinbased architecture into a multienzyme nanoreactor by incorporating the LigM aryl-O-demethylase originating from Sphingomonas paucimobilis SYK-6⁵⁶ as the second biocatalyst in our system. As detailed in the design scheme presented in Figure 5, our plan called for the non-covalent loading of LigM within DHFR*-decorated TmEs, thus artificially co-localizing the two enzymes in close spatial proximity relative to one another. In so doing, THF generated in situ from the reduction of DHF by surface-tethered DHFR* was expected to drive the THF-dependent demethylation of the aryl substrate vanillate by encapsulated LigM. The corresponding protocatechuate (PCA) formed from vanillate demethylation represents an industrially significant precursor on route to the high value synthons cis, cis-muconic acid and 2-pyrone-4,6-discarboxylate, which in turn are used in the mass production of nylon and biodegradable polymers. 72-⁷⁴ Similarly, the N⁵-methyltetrahydrofolate (5-CH₃-THF) produced upon methylation of THF represents an important biological supplement for the prevention of neonatal neural tube defects. 75-77 Metabolite exchange was expected to occur between the two biocatalysts in our nanocontainer-based system via the native pores located at the three distinct symmetry axes uniformly arrayed throughout the encapsulin shell.44

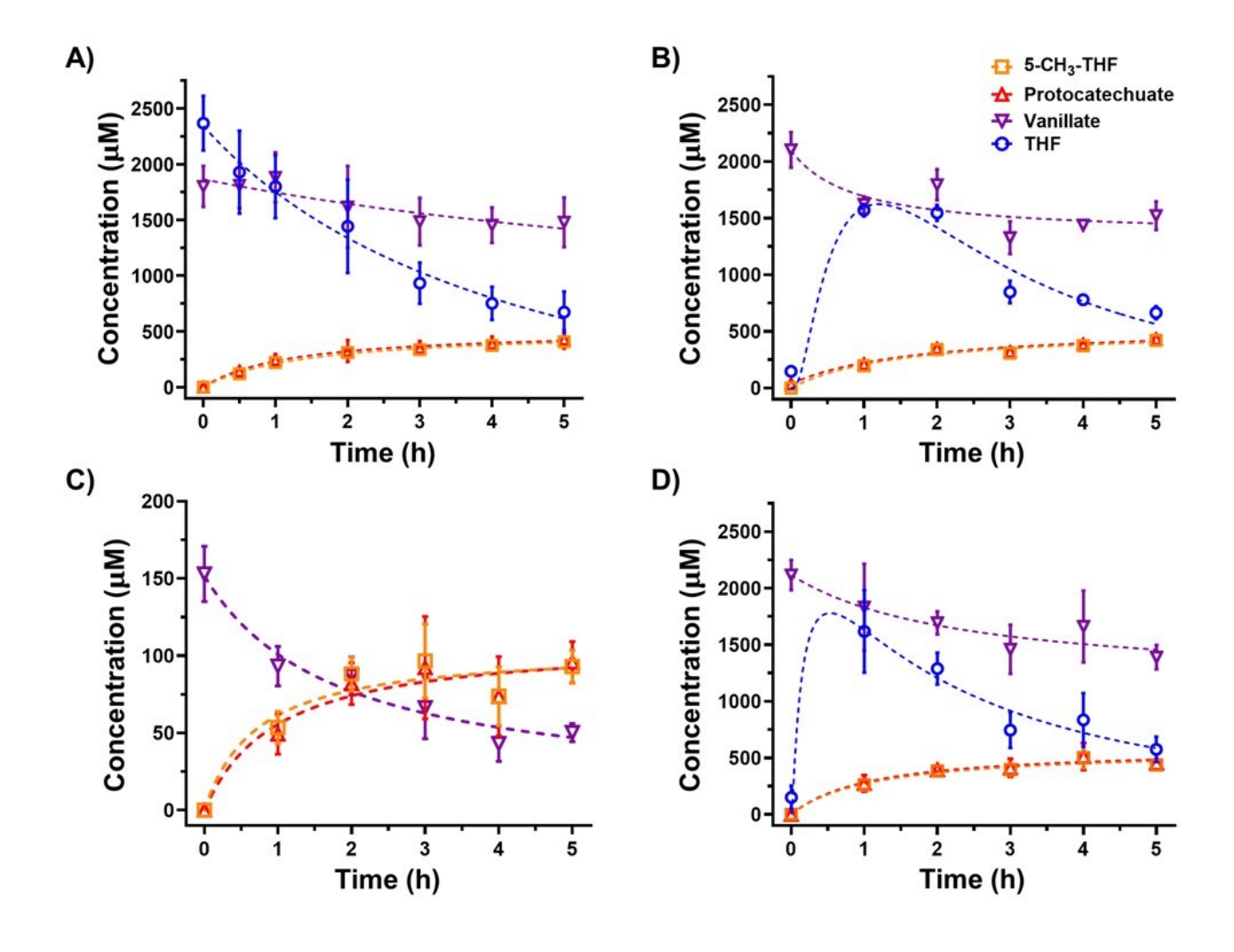


Figure 6. Enzymatic reactions monitoring the conversion of vanillate to PCA under different conditions. A) Conversion using LigM only with exogenous THF as the starting cofactor. B) Conversion using a 1:1 molar ratio of DHFR*-CST and LigM with DHF as the starting cofactor. C) Conversion of a starting concentration of 150 μM vanillate using a 1:1 molar ratio of DHFR*-CST and LigM to confirm product inhibition of LigM by 5-CH₃-THF. D) The same reaction as in B), but using a purified covalent bioconjugate of LigM-SC:DHFR*-CST. All reactions above used identical enzyme concentrations to permit direct comparison of data. Time point samples for all reactions were collected in triplicate with displayed error bars representing one standard deviation from the mean. The compound legend presented in the upper corner of chart B) applies to all charts depicted above.

Previous works have shown that non-native cargo can be directed into the TmE lumen using short aliphatic targeting peptides derived from the C-terminal region of the encapsulin's native ferritin-like protein (FLP) cargo.^{52, 55} As an initial test for our design strategy, we recombinantly fused the FLP's C-terminal cargo-loading peptide (Clp) onto the C-terminus of LigM and purified the resulting fusion protein to homogeneity (**Figure S10**). The demethylation activity of the purified LigM-Clp was subsequently assessed using exogenously added THF as the methyl acceptor, yielding the activity profile depicted in

Figure 6A. The resulting profile shows that the LigM-Clp fusion protein (referred to as LigM $^{\sim}$ from this point onward) retains enzymatic activity as approximately 20% conversion of the starting 2 mM vanillate is shown to occur over the 5 hour reaction period in the presence of 2 mM THF. In accordance with the inherent stoichiometry of the LigM-catalyzed demethylation reaction, the final PCA and 5-CH₃-THF products emerge in the expected 1:1 molar ratio. While the net conversion of the starting vanillate pool was relatively low, this result was not entirely unexpected as previous literature sources report that wildtype LigM is susceptible to product inhibition by 5-CH₃-THF with an apparent K_i value of 0.10 \pm 0.01 mM, representing a product binding affinity more than 7-fold stronger than the enzyme's reported K_m value of 0.72 \pm 0.11 mM for the THF cofactor.^{78, 79}

Using this activity data with LigM[~] alone as our baseline for comparison, we next performed an activity assay employing equimolar concentrations of purified DHFR*-CST and LigM[~] with exogenously added DHF as the starting cofactor to examine if the *in situ* generation of THF by DHFR*-CST could effectively drive the demethylase activity of LigM[~]. We elected to use DHFR*-CST for our metabolon assays with LigM[~] as its enzymatic activity is highly similar to that of DHFR*-NST and the presence of the SpyTag ligand on the C-terminus resulted in better overexpression of the enzyme *in vivo* relative to when the SpyTag was fused to the N-terminus. The resulting activity profile shows that the formation of THF is rapid as the starting pool of 2 mM DHF is completely depleted within the first hour of the reaction period (**Figure 6B**). However, while both the consumption of DHF and the corresponding formation of THF could be readily observed among the 259 nm absorbance signals detected during the LC/MS analysis of the various reaction components (**Figure S11**), direct quantitation of DHF concentrations proved difficult as DHF was found to rapidly degrade in response to the acidic quenching conditions used when collecting time point samples. This susceptibility of DHF to lower pH values has been documented previously and hampered us from effectively generating standard curves necessary for accurate cofactor

quantitation.^{80,81} Despite this inability to report DHF concentrations, standard curves for all other reaction components, including THF, could be generated with high accuracy (**Figure S12**).

Though the conversion of DHF to THF appeared to be rapid in the coupled enzyme reaction, the downstream conversion of vanillate to PCA by LigM⁻ appeared identical to the preceding reaction containing free LigM⁻ alone as roughly 20% total conversion was observed overall. To verify if the previously reported product inhibition by 5-CH₃-THF was indeed contributing to the overall throughput limitations exhibited by our coupled enzyme cascade, we subsequently prepared another activity assay, again containing a 1:1 molar ratio of DHFR*-CST and LigM⁻, using starting concentrations of 150 μM vanillate as the substrate and 2 mM DHF as the cofactor. This assay was designed to mimic reported conditions in which an excess of THF was able to overcome the higher binding affinity of the 5-CH₃-THF generated by wildtype LigM during the reaction period.⁷⁹ The resulting reaction profile generated with the reduced concentration of vanillate showed better conversion over the previous trials with more than 60% of the vanillate pool converted to PCA and 5-CH₃-THF within 5 hours (**Figure 6C**, full reaction profile presented in **Figure S13**), indicating that product inhibition is indeed the cause of the approximately 20% conversion cap for the preceding reactions containing equimolar concentrations of the appropriate cofactor and vanillate substrate.

In addition to the product inhibition by 5-CH₃-THF, we noticed upon closer examination of our enzymatic activity data that the decline in THF concentration during the 5 hour reaction period was consistently greater than the amount of 5-CH₃-THF produced, indicating that the THF pool was being prematurely depleted and was perhaps also hampering the demethylase activity of LigM. THF is well known to be susceptible to oxidative degradation by molecular oxygen under aerobic conditions, resulting in cleavage of the C^9 -N¹⁰ bond joining the cofactor's pterin and *p*-aminobenzoic acid moieties to form 6-formylpterin and *p*-(aminobenzoyl)-L-glutamate (*p*-ABG) as degradation byproducts (**Figure S14**)^{82,83}

Though excess sodium ascorbate salts were included in our reactions to serve as sacrificial oxidants intended to preserve the folate cofactor pools, we reassessed the raw LC/MS chromatograms from our activity assay datasets and located a product peak with a retention time of 5.1 minutes presenting positive and negative mode ion products directly corresponding to the molecular weight of *p*-ABG (**Figure S14**). We subsequently performed parallel activity assays under aerobic and anaerobic conditions using a 1:1 molar ratio of purified DHFR*-CST and LigM, the results of which show that the THF pool appears to be much more stable and the accumulation of *p*-ABG is significantly reduced under anaerobic conditions (**Figure S15**). However, despite the enhanced preservation of the THF pool under anaerobic conditions, again only about 20% of the starting vanillate substrate was converted into product over 5 hours, indicating that the product inhibition by 5-CH₃-THF is the primary factor affecting the catalytic activity of LigM in our assays (data not shown).

Given the observed product inhibition by 5-CH₃-THF, we also sought to determine whether reducing the spatial proximity between the two metabolon biocatalysts could influence the overall flux through the two-step cascade by generating sufficiently high local concentrations of THF to compensate for its weaker binding affinity with LigM. Consequently, we genetically fused the SpyCatcher domain onto the C-terminus of LigM to generate a LigM-SpyCatcher (LigM-SC) variant that would permit us the ability to covalently tether LigM directly to DHFR*-CST via isopeptide bond formation. Clarified cell lysates derived from separate heterologous expression cultures of LigM-SC and DHFR*-CST were mixed *in vitro* to effect covalent bond formation (**Figure S16**). Following a brief incubation period, the conjugated LigM-SC:DHFR*-CST complex was isolated as a homogeneously pure product through several sequential chromatography steps. However, a subsequent activity assay performed with these covalently-tethered biocatalysts in the presence of 2 mM starting pools of vanillate and DHF again yielded approximately 20% total conversion over the 5 hour incubation period (**Figure 6D**). While these results

indicate that the close spatial proximity of the two enzymes alone cannot overcome the 5-CH₃-THF inhibition of LigM to enhance the overall flux through the multistep catalytic pathway, Rosini *et al.* recently reported the successful diminution of LigM product inhibition using an enzyme-based THF cofactor regeneration system. ⁷⁹ Specifically, 5-CH₃-THF was recycled back to THF using a plant-derived methionine synthase that natively utilizes 5-CH₃-THF as a methyl donor to facilitate the methylation of L-homocysteine to L-methionine. Future expansion of our synthetic metabolon to include a similar cofactor regeneration system would likely enhance metabolon throughput in a likewise manner for increased production of the PCA precursor synthon.

Assessment of encapsulin-scaffolded metabolon performance

Considering the good agreement of the preceding three activity assay datasets generated when equimolar concentrations of substrate and cofactor were used to fuel the reaction cascade, we subsequently sought to probe the relative efficiency of our bi-enzymatic nanoreactor scaffold design. Based on the published crystal structures for both LigM^{78, 84} and TmE⁴⁴, we estimated that a theoretical maximum of 32 LigM monomers could be packaged within each nanocontainer given an approximate volume of 128 nm³ for each LigM enzyme and a luminal void volume of 4189 nm³ for the assembled encapsulins. Though this theoretical maximum would likely never be reached in practice due to steric constraints within the encapsulin lumen, the combination of these estimates and our ability to achieve full covalent decoration of TmE-SC nanocontainers with 60 immobilized DHFR* enzymes per container indicate that our multienzyme system should have an approximate minimum ratio of 2:1 DHFR* to LigM enzymes upon assembly. Nanoreactors were subsequently constructed by first co-expressing TmE-SC and LigM⁻ (TmE-encapsulated LigM⁻ referred to herein as TmE-SC•LigM), and then decorating the exterior surface of the nanocontainers in vitro by mixing the resulting clarified lysate from the TmE-SC•LigM culture with

clarified lysate derived from an expression culture containing DHFR*-CST to avoid the metabolic burdens of expressing all three proteins in a single host. Due to the large culture sizes needed to achieve sufficient yields of the three protein components, the nanoreactors were only semi-purified following several chromatography and salt-mediated precipitation steps. However, distinct protein bands corresponding to the sizes of the encapsulated LigM⁻ enzyme and the TmE-SC:DHFR*-CST fusion proteins were detectable via SDS-PAGE analysis following size exclusion chromatography (**Figure S17A**). The concentration of the encapsulated LigM⁻ population was subsequently determined by gel densitometry analysis (**Figure S17B**) and served as the basis for the preparation of our activity assays given that LigM⁻ represents the rate-limiting enzyme in the cascade reaction. The concentration of surface-immobilized DHFR*-CST was not directly measured, but rather it was qualitatively assumed that all available SpyCatcher domains were occupied given that an excess of DHFR*-CST was present following *in vitro* bioconjugation and no protein band corresponding to the molecular weight of unoccupied TmE-SC was visible in SDS-PAGE gels following the various purification steps (**Figure S17A**).

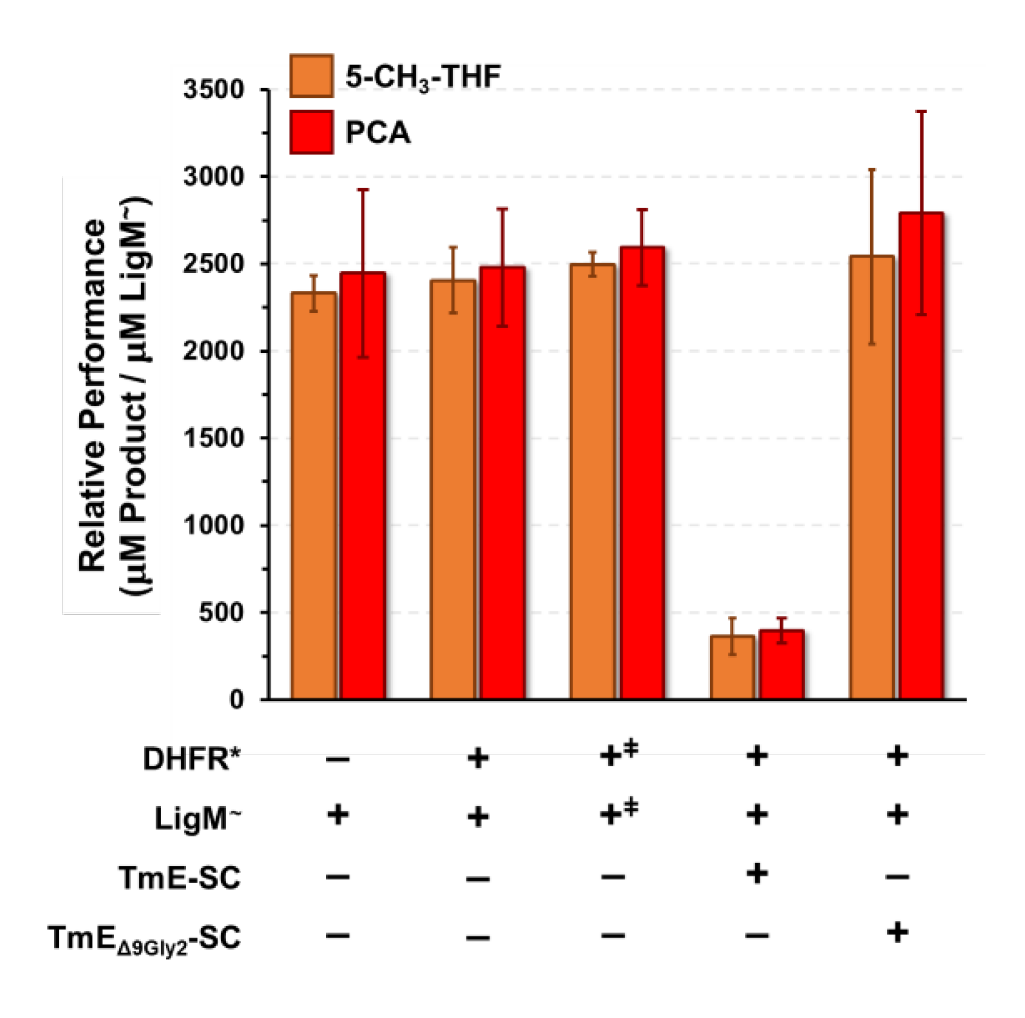


Figure 7. Performance assessment of synthetic metabolons. Reaction data were endpoint normalized by dividing the final concentration of a product chemical (5-CH₃-THF or PCA) after 5 hours of reaction time by the concentration of the rate-limiting enzyme (LigM⁻) used in the reaction. The ‡ symbol for the third set of data bars indicate that the DHFR* and LigM⁻ enzymes were covalently bioconjugated to one another via fused SpyTag and SpyCatcher elements, respectively.

Activity assays performed with DHFR*-decorated TmE-SC•LigM nanoreactors (i.e. TmE-SC•LigM:DHFR*-CST) show that the bi-enzymatic cascade is indeed functional as DHF was readily converted to THF, and the concentrations of both PCA and 5-CH₃-THF were observed to gradually increase in a linear fashion over the 5 hour reaction timeframe. However, in comparison to the preceding reaction profiles, encapsulation of LigM[~] leads to an apparent 5-fold reduction in cascade efficiency when the final amounts of PCA and 5-CH₃-THF are normalized relative to the concentration of LigM[~] present (**Figure 7**). We reasoned that this inefficiency was likely due to either some percentage of the encapsulated LigM[~] enzymes being inactive (either from protein denaturation or due to crowding within the encapsulin

lumen), or due to restricted diffusion of the bulky substrates and folate cofactors through the narrow 3 Å pores of the native encapsulin shell. The latter phenomenon has been reported previously for encapsulin-based systems, such as a ~1000-fold reduction in turnover observed for firefly luciferase encapsulated within a similarly sized encapsulin nanocontainer isolated from *Rhodococcus erythropolis* N771 due to the restricted diffusion of the required adenosine triphosphate and D-luciferin substrates into the encapsulin lumen. Fortuitously, our lab has previously generated an encapsulin variant, referred to as $TmE_{\Delta 9Gily2}$, possessing artificially enlarged pores located at the container's 5-fold symmetry axes which have been shown to allow for the enhanced diffusion of small cation probes across the encapsulin shell relative to the wildtype TmE containers. We thus recombinantly introduced the same $\Delta 9Gily2$ pore mutations into the TmE-SC gene sequence (new variant referred to as $TmE_{\Delta 9Gily2}$ -SC) to examine if the diffusion of substrates and/or cofactors was indeed the source of the poor performance exhibited by our nanoreactors.

DHFR*-decorated TmE_{Δ9Gly2}-SC•LigM nanoreactors were prepared and purified in the same fashion as the preceding nanoreactors containing wildtype-sized pores. Excitingly, activity assay data collected for the TmE_{Δ9Gly2}-SC•LigM:DHFR*-CST scaffolds showed a complete recovery of cascade efficiency as the LigM~-normalized endpoint concentrations of PCA and 5-CH₃-THF matched those obtained for all three of the assays performed with non-encapsulated LigM~ enzymes (**Figure 7**). These results indicate that restricted metabolite exchange was likely the cause of the inefficiency exhibited by the initial TmE-SC•LigM nanoreactor scaffolds containing wildtype-sized pores. Additionally, the recovery of cascade efficiency further indicated that the entire population of LigM~ enzymes within the TmE_{Δ9Gly2}-SC•LigM nanoreactors are catalytically competent, and thus the physical sequestration of LigM~ enzymes within the encapsulin lumen does not negatively impact enzymatic function. However, as with the activity assay performed using conjugated LigM-SC:DHFR*-CST fusion proteins, the co-

localization of the two biocatalysts in our nanoreactor-based metabolon design appears to offer no evidence of pathway flux enhancements relative to the reactions performed with both enzymes freely dispersed in solution.

CONCLUSION

In this study, we have successfully constructed a multienzyme nanoreactor system utilizing the T. maritima encapsulin as a bifunctional scaffold for the simultaneous surface display of one enzyme in tandem with the specific encapsulation of another. This particular metabolon design was chosen in an attempt to expand upon previously reported works in which multiple biocatalysts were either surface immobilized onto or co-encapsulated within nanocontainers exclusively. Our work reported herein exemplifies that successful and efficient cross-talk can be achieved between the two scaffolded biocatalysts while maintaining a physical barrier between them, a design feature which may prove useful for future endeavors in which users wish to employ functionally related catalysts that are incompatible in a traditional one-pot manner, such as certain biocatalyst and chemocatalyst species. 86,87 Additionally, our engineering efforts further typify the general stability and plasticity of encapsulins for biotechnology pursuits as recombinant fusion of the SpyCatcher domain onto the TmE monomer sequence was well tolerated, yielding fully assembled nanocontainers that adopt wildtype-like morphologies. Covalent immobilization of up to 60 DHFR enzymes onto encapsulin surfaces was similarly tolerated with no apparent negative impacts on the nanocontainers' assembly behavior and with minimal impacts on the catalytic function of surface-bound DHFRs. Indeed, the ability of TmE nanocontainers to tolerate both genetic fusion of SpyCatcher domains and the subsequent bioconjugation of either sfGFP or DHFR enzymes implies that the direct fusion of full proteins onto the encapsulin's C-terminus may be a viable route for future engineering efforts aimed at exterior surface display. However, it is worth noting that both the DHFR and sfGFP used herein are relatively small, monomeric proteins. Attempts to either fuse or immobilize larger or multimeric proteins onto encapsulin surfaces may require additional design considerations to avoid detrimental consequences with respect to encapsulin stability, fusion protein functionality, or both.

In terms of catalytic throughput, our encapsulin-templated metabolon was indeed functional, though it was initially shown to perform roughly 5 times slower than when the same two metabolon enzymes were freely dispersed in solution due to restricted metabolite diffusion across the nanocontainer shell. We subsequently eliminated the observed reduction in metabolon efficiency by recombinantly enlarging the 5-fold symmetry pores of the assembled encapsulins using a mutagenesis strategy reported previously. Additionally, consistent product inhibition by LigM-generated 5-CH₃-THF was shown to limit the net throughput of all the metabolon permutations we tested, though this effect could likely be ameliorated by introducing a cofactor regeneration system designed to eliminate the accumulation of 5-CH₃-THF in accordance with recent reports. The capacity to limit 5-CH₃-THF concentrations in future encapsulin-based metabolon designs would likely yield not only significantly enhanced metabolite flux levels, but it might also reveal synergistic cascade catalysis effects due to the close spatial proximity of the two catalysts that have been effectively masked in our current nanoreactor system. Nevertheless, the encapsulin engineering we present here further exemplifies the applicability of both encapsulins and proteinaceous nanocontainers in general as tailorable scaffolds for diverse biotechnology applications.

MATERIALS AND METHODS

Reagents and General Materials:

Fluroescein methotrexate triammonium salt was purchased from Biotium. Vanillate and protocatechuate were purchased from Oakwood Chemical. Tetrahydrofolate and N⁵-

methyltetrahydrofolate were purchased from Cayman Chemical. All other chemicals and reagents were purchased from Millipore Sigma. Carbon film 200 mesh copper electron microscopy grids were purchased from Electron Microscopy Sciences.

In vitro Conjugation Reactions

In vitro conjugations between purified proteins with fused SpyCatcher domains and partner proteins presenting fused SpyTags were performed by mixing a given final concentration of the SpyCatcher fusion protein with a minimum of a 5 μM excess of the SpyTag-fusion partner. All conjugation reactions were performed in 50 mM K-Phosphate (pH 7.0), 100 mM NaCl, 2.5 mM β-mercaptoethanol. Conjugation reactions with DHFR-SpyTag variants were carried out overnight at 4 °C while reactions with sfGFP-SpyTag were carried out for one hour at 4 °C as prolonged incubation was found to promote aggregation of the decorated nanocontainers. Purification of bioconjugates from unreacted starting proteins was performed by loading the conjugation reaction mixture into a SuperdexTM 200 Increase 10/300 GL column that had been pre-equilibrated with 50 mM K-Phosphate (pH 7.5), 100 mM NaCl, 2.5 mM β-mercaptoethanol and was connected to an ÄKTA Explorer 10 FPLC system. The same buffer was used as the mobile phase during purification chromatography, and protein clution was monitored spectrophotometrically at 280 nm. For samples containing sfGFP-ST, sample elution was also monitored at 485 nm to detect sfGFP chromophores. Purified bioconjugates were kept at 4 °C until needed for experimentation.

Fluorescence Titrations

Fluorescein methotrexate (MTX-F) titrations were performed by titrating purified sample proteins with known concentrations of MTX-F in 50 mM K-Phosphate, 0.1 M NaCl, 2.5 mM β-mercaptoethanol

and monitoring the change in fluorescence intensity at 517 nM upon MTF-F binding. The range of MTX-F tested spanned from $0.2-5.0~\mu\text{M}$. All fluorometric readings were collected using a HORIBA Jobin Yvon FluoroMax®-3 fluorimeter. Samples were excited at 496 nm and the resulting emission data were collected with both the excitation and emission slits of the instrument set at 2 nm and the data integration time set to 0.2 seconds. Segmented regression analysis of titration data was performed using GraphPad Prism 8.4.1.

Michaelis-Menten Kinetics Analyses

Steady-state kinetics of free and bioconjugated DHFR variants were performed at 22 °C by monitoring the depletion of NADPH spectrophotometrically at 340 nm on a Varian Cary 50 Bio UV-visible spectrophotometer. The reaction mixture used for all kinetics runs consisted of 100 mM K-Phosphate (pH 7.0), 100 mM NaCl, 1 mM dithiothreitol, 20 mM sodium ascorbate, and 0.1 mM NADPH. A final concentration of free DHFR* or bioconjugated DHFR* between 2.5 – 50 nM was added into the reaction mixture and allowed to equilibrate for at least 10 minutes to prevent hysteresis effects. Kinetics tests were initiated upon the addition of dihydrofolate (DHF) into the reaction mixture. A combined extinction coefficient for NADPH and DHF of 11,800 M⁻¹cm⁻¹ was used to calculate the rate of NADPH consumption during the course of each reaction. 88 All reactions were conducted in triplicate with error values representing one standard deviation from the mean. Kinetics data were processed using GraphPad Prism 8.4.1.

Thrombolytic Cleavage of Conjugates

Thrombin cleavage tests were performed at 100 µL scale in aqueous buffer consisting of 50 mM HEPES-KOH (pH 7.5), 150 mM NaCl. Samples of purified DHFR*-NST or TmE nanocontainers

possessing surface-tethered DHFR*-NST enzymes (10 μM final concentration) were incubated with 150 units of bovine thrombin at 4 °C for 16 hours. Cleavage-based liberation of DHFR* enzyme was assessed via 12% SDS-PAGE. For Michaelis-Menten analyses of thrombin-cleaved DHFR*, the thrombin reaction was scaled up to 300 μL, and then liberated DHFR* was isolated by loading the entire reaction mixture into a SuperdexTM 200 Increase 10/300 GL column and performing size exclusion chromatography on an ÄKTA Explorer 10 FPLC system. The size exclusion column was pre-equilibrated with 50 mM HEPES-KOH (pH 7.5), 150 mM NaCl prior to sample loading, and the same buffer was used as the mobile phase during sample separation. Isolated DHFR* enzyme was immediately used for Michaelis-Menten kinetics assays.

LC/MS Analyses

Multienzyme cascade activity assays were performed at either 37 °C under aerobic or anaerobic conditions using a reaction mixture containing 100 mM K-Phosphate (pH 7.0), 100 mM NaCl, 2 mM dithiothreitol, 5 mM sodium ascorbate, 3 mM NADPH, 2 mM DHF, and 2 mM vanillate. For the conversion reactions performed with LigM in the absence of DHFR*-CST, the reaction mixture was identical except that the NADPH was excluded and 2 mM THF was added in place of the DHF. Time point samples (35 μL each) were collected every hour for 5 hours. Each time point was immediately quenched by adding an equal volume of 240 mM HCl to the sample and mixing thoroughly. Samples were subsequently subjected to LC/MS analysis by injecting 50 μL of each quenched mixture into a Shimadzu LCMS-2020 Single Quadrupole Liquid Chromatograph Mass Spectrometer equipped with an Agilent Zorbax Eclipse Plus C-18 column (5 μm particle size; 4.6 x 250 mm). Sample chromatography was performed at a flow rate of 1.5 mL·min⁻¹. The mobile phase consisted of a mixture of (A) acetonitrile with 0.1% (v/v) formic acid and (B) water with 0.1% (v/v) formic acid. For compound separation, the following

mobile phase gradient was used: 0 minutes, 5% **A**; 0.1 to 15 minutes, linear gradient from 5% to 20% **A**; 15.1 to 25 minutes, 5% **A** to re-equilibrate the column for subsequent injections. Elution of reaction components was monitored at 259 nm, and the retention times for the components were as follows: THF (5.6 min); 5-CH₃-THF (6.4 min); protocatechuate (7.7 min); DHF (9.9 min); vanillate (12.5 min). For mass spectroscopy analysis, the interface temperature was set at 350 °C, the drying line was set at 250 °C, and the heat block was set at 200 °C. Nitrogen gas was used as both the nebulizing and drying gas, and the respective flow rates for the nebulizing and drying lines were 1.5 and 3.0 L·min⁻¹, respectively. All reactions were conducted in triplicate with error values representing one standard deviation from the mean. Curve fits for all activity assays were generated using GraphPad Prism 8.4.1.

Transmission Electron Microscopy Imaging:

Individual TEM grids were prepared by applying 4 μ L of biological sample onto the carbon surface of carbon-copper grids for five minutes. Samples were diluted to a final protein concentration between 0.1 - 0.3 mg/mL to prevent overcrowding of proteins on the grid surface. After five minutes had elapsed, the edge of each grid was gently blotted against a sheet of Whatman 1 filter paper. Each grid was then inverted, and the carbon surface was quickly immersed sequentially into two drops of deionized water. The edge of the grid was again blotted against filter paper, and then negative staining was accomplished by applying 4 μ L of 1% (w/v) phosphotungstic acid (pH 6.5, prepared in double distilled water and pH adjusted with KOH) onto the surface of the grid. After 20 seconds had elapsed, the edge of each grid was then blotted against filter paper one final time, and then the grids were allowed to air dry for five minutes before being placed into a vacuum desiccator for five additional minutes. TEM imaging was performed on a Hitachi HT7700 transmission electron microscope operating at an accelerating voltage of 80.0 kV.

ASSOCIATED CONTENT

Supporting Information

Experimental details for cloning, protein expression and purification, and data pertaining to

bioconjugation reactions, fluorescence titrations, LC/MS assays and standards, and gel densitometry

analyses.

AUTHOR INFORMATION

Corresponding Author

Stefan Lutz – Codexis Inc., 200 Penobscot Drive, Redwood City, California 94063, United States.

ORCID: 0000-0003-1043-0162

E-mail: stefan.lutz@codexis.com

Author

Matthew Jenkins – School of Chemistry and Biochemistry, Georgia Institute of Technology,

Atlanta, Georgia 30306, United States. ORCID: 0000-0002-0583-3533

CONFLICT OF INTEREST

The authors declare no competing financial interest.

ACKNOWLEDGEMENTS

This work was funded in part by grants from the Emory University Research Committee and the

U.S. National Science Foundation (CBET- 1706891). The authors thank Prof. Vincent Conticello for the

sfGFP and SpyCatcher genes, Dr. Elsie Williams and Dr. Spencer Hughes for assistance with the

collection of TEM images, and all members of the Lutz lab for their help and support during the preparation of this manuscript.

REFERENCES

- (1) Douglas, T., and Young, M. (2006) Viruses: making friends with old foes. Science. 312, 873-875.
- (2) Andrews, S. C. (2010) The Ferritin-like superfamily: Evolution of the biological iron storeman from a rubrerythrin-like ancestor. *Biochim. Biophys. Acta 1800*, 691-705.
- (3) Yeates, T. O., Crowley, C. S., and Tanaka, S. (2010) Bacterial microcompartment organelles: protein shell structure and evolution. *Ann. Rev. Biophys.* 39, 185-205.
- (4) Cornejo, E., Abreu, N., and Komeili, A. (2014) Compartmentalization and organelle formation in bacteria. *Curr. Opin. Cell Biol.* 26, 132-138.
- (5) Bobik, T. A., Lehman, B. P., and Yeates, T. O. (2015) Bacterial microcompartments: widespread prokaryotic organelles for isolation and optimization of metabolic pathways. *Mol. Microbiol.* 98, 193-207.
- (6) Giessen, T. W., and Silver, P. A. (2017) Widespread distribution of encapsulin nanocompartments reveals functional diversity. *Nat. Microbiol.* 2, 17029.
- (7) Schwarz, B., Uchida, M., and Douglas, T. (2017) Biomedical and Catalytic Opportunities of Virus-Like Particles in Nanotechnology. *Adv. Virus Res.* 97, 1-60.
- (8) Aumiller, W. M., Uchida, M., and Douglas, T. (2018) Protein cage assembly across multiple length scales. *Chem. Soc. Rev.* 47, 3433-3469.
- (9) Diaz, D., Care, A., and Sunna, A. (2018) Bioengineering Strategies for Protein-Based Nanoparticles. *Genes* 9, 370.
- (10) Schoonen, L., and van Hest, J. C. M. (2014) Functionalization of protein-based nanocages for drug delivery applications. *Nanoscale* 6, 7124-7141.

- (11) Eiben, S., Koch, C., Altintoprak, K., Southan, A., Tovar, G., Laschat, S., Weiss, I. M., and Wege, C. (2019) Plant virus-based materials for biomedical applications: Trends and prospects. *Adv Drug Deliv Rev.* 145, 96-118.
- (12) Lopez-Gallego, F., and Schmidt-Dannert, C. (2010) Multi-enzymatic synthesis. *Curr. Opin. Chem. Biol.* 14, 174-183.
- (13) Muschiol, J., Peters, C., Oberleitner, N., Mihovilovic, M. D., Bornscheuer, U. T., and Rudroff, F. (2015) Cascade catalysis strategies and challenges en route to preparative synthetic biology. *Chem. Comm.* 51, 5798-5811.
- (14) Lee, H., DeLoache, W. C., and Dueber, J. E. (2012) Spatial organization of enzymes for metabolic engineering. *Metab. Eng.* 14, 242-251.
- (15) Schoffelen, S., and van Hest, J. C. M. (2012) Multi-enzyme systems: bringing enzymes together *in vitro*. *Soft Matter 8*, 1736-1746.
- (16) Quin, M. B., Wallin, K. K., Zhang, G., and Schmidt-Dannert, C. (2017) Spatial organization of multi-enzyme biocatalytic cascades. *Org. Biomol. Chem.* 15, 4260-4271.
- (17) Ljungcrantz, P., Carlsson, H., Mansson, M. O., Buckel, P., Mosbach, K., and Buelow, L. (1989) Construction of an artificial bifunctional enzyme, β-galactosidase/galactose dehydrogenase, exhibiting efficient galactose channeling. *Biochemistry* 28, 8786-8792.
- (18) Seo, H. S., Koo, Y. J., Lim, J. Y., Song, J. T., Kim, C. H., Kim, J. K., Lee, J. S., and Choi, Y. D. (2000) Characterization of a Bifunctional Enzyme Fusion of Trehalose-6-Phosphate Synthetase and Trehalose-6-Phosphate Phosphatase of *Escherichia coli. Appl. Environ. Microbiol.* 66, 2484.
- (19) Dueber, J. E., Wu, G. C., Malmirchegini, G. R., Moon, T. S., Petzold, C. J., Ullal, A. V., Prather, K. L. J., and Keasling, J. D. (2009) Synthetic protein scaffolds provide modular control over metabolic flux. *Nat. Biotechnol.* 27, 753-U107.

- (20) Fu, J., Yang, Y. R., Johnson-Buck, A., Liu, M., Liu, Y., Walter, N. G., Woodbury, N. W., and Yan, H. (2014) Multi-enzyme complexes on DNA scaffolds capable of substrate channelling with an artificial swinging arm. *Nat. Nanotechnol. 9*, 531-536.
- (21) Moon, T. S., Dueber, J. E., Shiue, E., and Prather, K. L. (2010) Use of modular, synthetic scaffolds for improved production of glucaric acid in engineered *E. coli. Metab. Eng. 12*, 298-305.
- (22) Wilner, O. I., Weizmann, Y., Gill, R., Lioubashevski, O., Freeman, R., and Willner, I. (2009) Enzyme cascades activated on topologically programmed DNA scaffolds. *Nat. Nanotechnol.* 4, 249-254.
- (23) McConnell, S. A., Cannon, K. A., Morgan, C., McAllister, R., Amer, B. R., Clubb, R. T., and Yeates, T. O. (2020) Designed Protein Cages as Scaffolds for Building Multienzyme Materials. *ACS Synth. Biol. 9*, 381-391.
- (24) Kim, S., and Hahn, J. S. (2014) Synthetic scaffold based on a cohesin-dockerin interaction for improved production of 2,3-butanediol in *Saccharomyces cerevisiae*. *J. Biotechnol.* 192 Pt A, 192-196.
- (25) Krzek, M., van Beek, H. L., Permentier, H. P., Bischoff, R., and Fraaije, M. W. (2016) Covalent immobilization of a flavoprotein monooxygenase via its flavin cofactor. *Enzyme Microb. Technol.* 82, 138-143.
- (26) Velasco-Lozano, S., Benítez-Mateos, A. I., and López-Gallego, F. (2017) Co-immobilized Phosphorylated Cofactors and Enzymes as Self-Sufficient Heterogeneous Biocatalysts for Chemical Processes. *Angew. Chem. Int., Ed. Engl.* 56, 771-775.
- (27) Hwang, E. T., and Lee, S. (2019) Multienzymatic Cascade Reactions via Enzyme Complex by Immobilization. *ACS Catal.* 9, 4402-4425.
- (28) Matsumoto, R., Kakuta, M., Sugiyama, T., Goto, Y., Sakai, H., Tokita, Y., Hatazawa, T., Tsujimura, S., Shirai, O., and Kano, K. (2010) A liposome-based energy conversion system for accelerating the multi-enzyme reactions. *Phys. Chem. Chem. Phys.* 12, 13904-13906.

- (29) Myhrvold, C., Polka, J. K., and Silver, P. A. (2016) Synthetic Lipid-Containing Scaffolds Enhance Production by Colocalizing Enzymes. *ACS Synth. Biol.* 5, 1396-1403.
- (30) Alves, N. J., Turner, K. B., Daniele, M. A., Oh, E., Medintz, I. L., and Walper, S. A. (2015) Bacterial Nanobioreactors--Directing Enzyme Packaging into Bacterial Outer Membrane Vesicles. *ACS Appl. Mater. Interfaces* 7, 24963-24972.
- (31) Vriezema, D. M., Garcia, P. M. L., Sancho Oltra, N., Hatzakis, N. S., Kuiper, S. M., Nolte, R. J. M., Rowan, A. E., and van Hest, J. C. M. (2007) Positional Assembly of Enzymes in Polymersome Nanoreactors for Cascade Reactions. *Angew. Chem. Int. Ed.* 46, 7378-7382.
- (32) Azuma, Y., Zschoche, R., Tinzl, M., and Hilvert, D. (2016) Quantitative Packaging of Active Enzymes into a Protein Cage. *Angew. Chem. Int. Ed.* 55, 1531-1534.
- (33) Liang, M., Frank, S., Lunsdorf, H., Warren, M. J., and Prentice, M. B. (2017) Bacterial microcompartment-directed polyphosphate kinase promotes stable polyphosphate accumulation in *E. coli*. *Biotechnol. J. 12*, 1600415.
- (34) O'Neil, A., Prevelige, P. E., and Douglas, T. (2013) Stabilizing viral nano-reactors for nerve-agent degradation. *Biomater. Sci. 1*, 881-886.
- (35) Patterson, D. P., Prevelige, P. E., and Douglas, T. (2012) Nanoreactors by Programmed Enzyme Encapsulation Inside the Capsid of the Bacteriophage P22. *ACS Nano 6*, 5000-5009.
- (36) Plegaria, J. S., and Kerfeld, C. A. (2018) Engineering nanoreactors using bacterial microcompartment architectures. *Curr. Opin. Biotechnol.* 51, 1-7.
- (37) Renggli, K., Baumann, P., Langowska, K., Onaca, O., Bruns, N., and Meier, W. (2011) Selective and Responsive Nanoreactors. *Adv. Funct. Mater.* 21, 1241-1259.

- (38) Aljabali, A. A. A., Barclay, J. E., Steinmetz, N. F., Lomonossoff, G. P., and Evans, D. J. (2012) Controlled immobilisation of active enzymes on the cowpea mosaic virus capsid. *Nanoscale 4*, 5640-5645.
- (39) Koch, C., Wabbel, K., Eber, F. J., Krolla-Sidenstein, P., Azucena, C., Gliemann, H., Eiben, S., Geiger, F., and Wege, C. (2015) Modified TMV Particles as Beneficial Scaffolds to Present Sensor Enzymes. *Front. Plant Sci.* 6, 1137.
- (40) Wei, Q., He, S., Qu, J., and Xia, J. (2020) Synthetic Multienzyme Complexes Assembled on Virus-like Particles for Cascade Biosynthesis *In Cellulo. Bioconjug. Chem.* 31, 2413-2420.
- (41) Lawrence, A. D., Frank, S., Newnham, S., Lee, M. J., Brown, I. R., Xue, W.-F., Rowe, M. L., Mulvihill, D. P., Prentice, M. B., Howard, M. J., and Warren, M. J. (2014) Solution Structure of a Bacterial Microcompartment Targeting Peptide and Its Application in the Construction of an Ethanol Bioreactor. *ACS Synth. Biol.* 3, 454-465.
- (42) Patterson, D. P., Schwarz, B., Waters, R. S., Gedeon, T., and Douglas, T. (2014) Encapsulation of an Enzyme Cascade within the Bacteriophage P22 Virus-Like Particle. *ACS Chem. Biol. 9*, 359-365.
- (43) Giessen, T. W., and Silver, P. A. (2016) A Catalytic Nanoreactor Based on *in Vivo* Encapsulation of Multiple Enzymes in an Engineered Protein Nanocompartment. *ChemBioChem 17*, 1931-1935.
- (44) Sutter, M., Boehringer, D., Gutmann, S., Guenther, S., Prangishvili, D., Loessner, M. J., Stetter, K. O., Weber-Ban, E., and Ban, N. (2008) Structural basis of enzyme encapsulation into a bacterial nanocompartment. *Nat. Struct. Mol. Biol.* 15, 939-947.
- (45) Wikoff, W. R., Liljas, L., Duda, R. L., Tsuruta, H., Hendrix, R. W., and Johnson, J. E. (2000) Topologically linked protein rings in the bacteriophage HK97 capsid. *Science* 289, 2129-2133.
- (46) Akita, F., Chong, K. T., Tanaka, H., Yamashita, E., Miyazaki, N., Nakaishi, Y., Suzuki, M., Namba, K., Ono, Y., Tsukihara, T., and Nakagawa, A. (2007) The Crystal Structure of a Virus-like Particle from

- the Hyperthermophilic Archaeon *Pyrococcus furiosus* Provides Insight into the Evolution of Viruses. *J. Mol. Biol.* 368, 1469-1483.
- (47) McHugh, C. A., Fontana, J., Nemecek, D., Cheng, N. Q., Aksyuk, A. A., Heymann, J. B., Winkler, D. C., Lam, A. S., Wall, J. S., Steven, A. C., and Hoiczyk, E. (2014) A virus capsid-like nanocompartment that stores iron and protects bacteria from oxidative stress. *EMBO J. 33*, 1896-1911.
- (48) Giessen, T. W., Orlando, B. J., Verdegaal, A. A., Chambers, M. G., Gardener, J., Bell, D. C., Birrane, G., Liao, M., and Silver, P. A. (2019) Large protein organelles form a new iron sequestration system with high storage capacity. *Elife* 8, e46070.
- (49) Lončar, N., Rozeboom, H. J., Franken, L. E., Stuart, M. C. A., and Fraaije, M. W. (2020) Structure of a robust bacterial protein cage and its application as a versatile biocatalytic platform through enzyme encapsulation. *Biochem. Biophys. Res. Commun.* 529, 548-553.
- (50) Nichols, R. J., Cassidy-Amstutz, C., Chaijarasphong, T., and Savage, D. F. (2017) Encapsulins: molecular biology of the shell. *Crit. Rev. Biochem. Mol. Biol.* 52 (5), 583-594.
- (51) Rurup, W. F., Snijder, J., Koay, M. S. T., Heck, A. J. R., and Cornelissen, J. (2014) Self-Sorting of Foreign Proteins in a Bacterial Nanocompartment. *J. Am. Chem. Soc.* 136, 3828-3832.
- (52) Cassidy-Amstutz, C., Oltrogge, L., Going, C. C., Lee, A., Teng, P., Quintanilla, D., East-Seletsky, A., Williams, E. R., and Savage, D. F. (2016) Identification of a Minimal Peptide Tag for *in Vivo* and *in Vitro* Loading of Encapsulin. *Biochemistry* 55, 3461-3468.
- (53) Tamura, A., Fukutani, Y., Takami, T., Fujii, M., Nakaguchi, Y., Murakami, Y., Noguchi, K., Yohda, M., and Odaka, M. (2015) Packaging Guest Proteins into the Encapsulin Nanocompartment from *Rhodococcus erythropolis* N771. *Biotechnol. Bioeng.* 112, 13-20.
- (54) Lau, Y. H., Giessen, T. W., Altenburg, W. J., and Silver, P. A. (2018) Prokaryotic nanocompartments form synthetic organelles in a eukaryote. *Nat. Commun.* 9, 1311.

- (55) Künzle, M., Mangler, J., Lach, M., and Beck, T. (2018) Peptide-directed encapsulation of inorganic nanoparticles into protein containers. *Nanoscale* 10, 22917-22926.
- (56) Abe, T., Masai, E., Miyauchi, K., Katayama, Y., and Fukuda, M. (2005) A tetrahydrofolate-dependent *O*-demethylase, LigM, is crucial for catabolism of vanillate and syringate in *Sphingomonas* paucimobilis SYK-6, *J. Bacteriol.* 187, 2030-2037.
- (57) Masai, E., Katayama, Y., and Fukuda, M. (2007) Genetic and biochemical investigations on bacterial catabolic pathways for lignin-derived aromatic compounds. *Biosci. Biotechnol. Biochem.* 71, 1-15.
- (58) Zakeri, B., Fierer, J. O., Celik, E., Chittock, E. C., Schwarz-Linek, U., Moy, V. T., and Howarth, M. (2012) Peptide tag forming a rapid covalent bond to a protein, through engineering a bacterial adhesin. *Proc. Natl. Acad. Sci. U.S.A. 109*, E690-697.
- (59) Kim, H., Choi, H., Bae, Y., and Kang, S. (2019) Development of target-tunable P22 VLP-based delivery nanoplatforms using bacterial superglue. *Biotechnol. Bioeng.* 116, 2843-2851.
- (60) Pedelacq, J. D., Cabantous, S., Tran, T., Terwilliger, T. C., and Waldo, G. S. (2006) Engineering and characterization of a superfolder green fluorescent protein. *Nat. Biotechnol.* 24, 79-88.
- (61) Shaw, D., Odom, J. D., and Dunlap, R. B. (1999) High expression and steady-state kinetic characterization of methionine site-directed mutants of *Escherichia coli* methionyl- and selenomethionyl-dihydrofolate reductase. *Biochim. Biophys. Acta* 1429, 401-410.
- (62) Ohmae, E., Fukumizu, Y., Iwakura, M., and Gekko, K. (2005) Effects of mutation at methionine-42 of *Escherichia coli* dihydrofolate reductase on stability and function: implication of hydrophobic interactions. *J. Bochem.* 137, 643-652.
- (63) Loveridge, E. J., Hroch, L., Hughes, R. L., Williams, T., Davies, R. L., Angelastro, A., Luk, L. Y. P., Maglia, G., and Allemann, R. K. (2017) Reduction of Folate by Dihydrofolate Reductase from *Thermotoga maritima*. *Biochemistry* 56, 1879-1886.

- (64) Rajagopalan, P. T., Zhang, Z., McCourt, L., Dwyer, M., Benkovic, S. J., and Hammes, G. G. (2002) Interaction of dihydrofolate reductase with methotrexate: ensemble and single-molecule kinetics. *Proc. Natl. Acad. Sci. U.S.A.* 99, 13481-13486.
- (65) Wang, L., Goodey, N. M., Benkovic, S. J., and Kohen, A. (2006) The role of enzyme dynamics and tunnelling in catalysing hydride transfer: studies of distal mutants of dihydrofolate reductase. *Phil. Trans. R. Soc. B* 361, 1307-1315.
- (66) Wang, L., Goodey, N. M., Benkovic, S. J., and Kohen, A. (2006) Coordinated effects of distal mutations on environmentally coupled tunneling in dihydrofolate reductase. *Proc. Natl. Acad. Sci.* 103, 15753-15758.
- (67) Gapski, G. R., Whiteley, J. M., Rader, J. I., Cramer, P. L., Henderson, G. B., Neef, V., and Huennekens, F. M. (1975) Synthesis of a fluorescent derivative of amethopterin. *J. Med. Chem.* 18, 526-528.
- (68) Degan, P., Carpano, P., Cercignani, G., and Montagnoli, G. (1989) A fluorescence study of substrate and inhibitor binding to bovine liver dihydrofolate reductase. *Int. J. Biochem.* 21, 291-295.
- (69) Jasensky, J., Ferguson, K., Baria, M., Zou, X., McGinnis, R., Kaneshiro, A., Badieyan, S., Wei, S., Marsh, E. N. G., and Chen, Z. (2018) Simultaneous Observation of the Orientation and Activity of Surface-Immobilized Enzymes. *Langmuir 34*, 9133-9140.
- (70) Hoarau, M., Badieyan, S., and Marsh, E. N. G. (2017) Immobilized enzymes: understanding enzyme surface interactions at the molecular level. *Org. Biomol. Chem.* 15, 9539-9551.
- (71) Xiong, Y., Huang, J., Wang, S.-T., Zafar, S., and Gang, O. (2020) Local Environment Affects the Activity of Enzymes on a 3D Molecular Scaffold. *ACS Nano 14* (11), 14646-14654.
- (72) Zhang, R., Zhao, C.-H., Chang, H.-C., Chai, M.-Z., Li, B.-Z., and Yuan, Y.-J. (2019) Lignin valorization meets synthetic biology. *Eng. Life Sci.* 19, 463-470.

- (73) Wu, W., Dutta, T., Varman, A. M., Eudes, A., Manalansan, B., Loque, D., and Singh, S. (2017) Lignin Valorization: Two Hybrid Biochemical Routes for the Conversion of Polymeric Lignin into Value-added Chemicals. *Sci. Rep.* 7, 8420.
- (74) Mori, K., Kamimura, N., and Masai, E. (2018) Identification of the protocatechuate transporter gene in *Sphingobium* sp. strain SYK-6 and effects of overexpression on production of a value-added metabolite. *Appl. Microbiol. Biotechnol.* 102, 4807-4816.
- (75) Scaglione, F., and Panzavolta, G. (2014) Folate, folic acid and 5-methyltetrahydrofolate are not the same thing. *Xenobiotica* 44, 480-488.
- (76) Pietrzik, K., Bailey, L., and Shane, B. (2010) Folic acid and L-5-methyltetrahydrofolate: comparison of clinical pharmacokinetics and pharmacodynamics. *Clin. Pharmacokinet.* 49, 535-548.
- (77) Obeid, R., Holzgreve, W., and Pietrzik, K. (2013) Is 5-methyltetrahydrofolate an alternative to folic acid for the prevention of neural tube defects? *J. Perinat. Med.* 41, 469-483.
- (78) Kohler, A. C., Mills, M. J. L., Adams, P. D., Simmons, B. A., and Sale, K. L. (2017) Structure of aryl-O-demethylase offers molecular insight into a catalytic tyrosine-dependent mechanism, *Proc. Natl. Acad. Sci. 114*, E3205.
- (79) Rosini, E., D'Arrigo, P., and Pollegioni, L. (2016) Demethylation of vanillic acid by recombinant LigM in a one-pot cofactor regeneration system. *Catal. Sci. Technol.* 6, 7729-7737.
- (82) Reed, L. S., and Archer, M. C. (1980) Oxidation of tetrahydrofolic acid by air. *J. Agric. Food Chem.* 28, 801-805.
- (80) Gazzali, A. M., Lobry, M., Colombeau, L., Acherar, S., Azaïs, H., Mordon, S., Arnoux, P., Baros, F., Vanderesse, R., and Frochot, C. (2016) Stability of folic acid under several parameters. *Eur. J. Pharm. Sci.* 93, 419-430.

- (81) De Brouwer, V., Zhang, G.-F., Storozhenko, S., Van Der Straeten, D., and Lambert, W. E. (2007) pH stability of individual folates during critical sample preparation steps in prevision of the analysis of plant folates. *Phytochem. Anal.* 18, 496-508.
- (83) Chippel, D., and Scrimgeour, K. G. (1970) Oxidative degradation of dihydrofolate and tetrahydrofolate. *Can. J. Biochem.* 48, 999-1009.
- (84) Harada, A., Kamimura, N., Takeuchi, K., Yu, H. Y., Masai, E., and Senda, T. (2017) The crystal structure of a new *O*-demethylase from *Sphingobium* sp. strain SYK-6. *FEBS J. 284*, 1855-1867.
- (85) Williams, E. M., Jung, S. M., Coffman, J. L., and Lutz, S. (2018) Pore Engineering for Enhanced Mass Transport in Encapsulin Nanocompartments. *ACS Synth. Biol.* 7, 2514-2517.
- (86) Rudroff, F., Mihovilovic, M. D., Gröger, H., Snajdrova, R., Iding, H., and Bornscheuer, U. T. (2018) Opportunities and challenges for combining chemo- and biocatalysis. *Nat. Catal.* 1, 12-22.
- (87) Köhler, V., Wilson, Y. M., Dürrenberger, M., Ghislieri, D., Churakova, E., Quinto, T., Knörr, L., Häussinger, D., Hollmann, F., Turner, N. J., and Ward, T. R. (2013) Synthetic cascades are enabled by combining biocatalysts with artificial metalloenzymes. *Nat. Chem.* 5, 93-99.
- (88) Stone, S. R., and Morrison, J. F. (1982) Kinetic mechanism of the reaction catalyzed by dihydrofolate reductase from *Escherichia coli*. *Biochemistry* 21, 3757-3765.